


Article

Sn(IV) Porphyrin-Based Ionic Self-Assembled Nanostructures and Their Application in Visible Light Photo-Degradation of Malachite Green

Nirmal Kumar Shee and Hee-Joon Kim * 

Department of Chemistry and Bioscience, Kumoh National Institute of Technology, Gumi 39177, Korea; nirmalshee@gmail.com

* Correspondence: hjk@kumoh.ac.kr; Tel.: +82-54-4787822

Abstract: A series of porphyrin-based ionic complexes were prepared through the reaction of two porphyrin precursors, 5,10,15,20-tetrakis(4-(2-pyridyl)phenyl)porphyrin H₂TPhPyP (**1**) and *trans*-dihydroxo [5,10,15,20-tetrakis(4-(2-pyridyl)phenyl)porphyrinato]tin(IV) Sn(OH)₂TPhPyP (**2**), with various acids (HCl, HNO₃, CF₃COOH, H₂SO₄, H₂CO₃, and H₃PO₄). The complexes were characterized via elemental analysis, ¹H nuclear magnetic resonance spectroscopy, electrospray ionization mass spectrometry, Fourier transform infrared (FT-IR) spectroscopy, ultraviolet (UV)-visible spectroscopy, fluorescence spectroscopy, and field-emission scanning electron microscopy (FE-SEM). Each compound exhibited different results for UV-visible, fluorescence, FT-IR, and FE-SEM studies depending on the counter anions. The complexes possessed different self-assembled nanostructures based on electronic interactions between the cations of compounds **1** and **2** with different counter anions. These aggregated species are stabilized by electrostatic forces and the π - π stacking interactions between the two porphyrin rings, in which the counter anions play an important bridging role. The counter anions also play an important role in controlling the morphology and photocatalytic properties of the as-developed materials. The complexes were then used for the photocatalytic degradation of the malachite green (MG) dye in aqueous media under visible light irradiation for up to 70 min. A morphology-dependent photocatalytic degradation of the MG dye was observed for all the ionic complexes, with efficiencies ranging from 50% to 95%.

Keywords: Sn(IV) porphyrin; ionic self-assembly; nanostructures; photocatalysts; photodegradation; malachite green



Citation: Shee, N.K.; Kim, H.-J. Sn(IV) Porphyrin-Based Ionic Self-Assembled Nanostructures and Their Application in Visible Light Photo-Degradation of Malachite Green. *Catalysts* **2022**, *12*, 799. <https://doi.org/10.3390/catal12070799>

Academic Editors: Roberto Comparelli, Ilaria De Pasquale and Chiara Lo Porto

Received: 1 July 2022

Accepted: 19 July 2022

Published: 20 July 2022

Publisher's Note: MDPI stays neutral with regard to jurisdictional claims in published maps and institutional affiliations.



Copyright: © 2022 by the authors. Licensee MDPI, Basel, Switzerland. This article is an open access article distributed under the terms and conditions of the Creative Commons Attribution (CC BY) license (<https://creativecommons.org/licenses/by/4.0/>).

1. Introduction

Agricultural and industrial activities generate significant amounts of toxic compounds that are discharged into water ecosystems, causing severe environmental issues. Large quantities of organic dyes, herbicides, phenols, pesticides, plasticizers, biphenyls, amino, and nitro compounds are discharged into water bodies, endangering aquatic life and water potability [1,2]. Several methods to remove hazardous pollutants from wastewater have been reported, including those based on physicochemical techniques, such as adsorption [3], membrane filtration [4], ion-exchange [5], chemical precipitation [6], electrolysis [7], and advanced oxidation processes (AOPs) [8]. Among them, AOPs are the most commonly used methods owing to their simple operation, high degradation rate without the generation of secondary pollutants, and degradation of the entire pollutant to less-toxic compounds (CO₂ and H₂O). These methods are based on the degradation of pollutant molecules by reactive oxygen species (ROS) generated in situ using a suitable photocatalyst. Photocatalysts absorb light from sunlight and generate ROS, which facilitate the degradation of organic pollutants in water [9–11]. TiO₂ has been used as a promising photocatalyst owing to its high stability, low toxicity, and high photocatalytic efficiency for the degradation of pollutants in water. However, a large band gap (~3.2 eV) restricts the use of TiO₂ to only

ultraviolet light ($\lambda < 370$ nm). In addition, the high recombination rate of photo-induced electron-hole pairs lower the quantum efficiency of photocatalytic processes [12,13].

Porphyrinoids (free-base porphyrins or metalloporphyrins) can be used as alternatives to TiO_2 as they have a high absorption efficiency through a wider wavelength range (in the UV-vis region). However, the use of porphyrinoids in homogeneous catalysis has drawbacks, which include the aggregation of porphyrin in solution, low reusability, and poor recovery from the reaction mixture. To overcome these challenges, porphyrin-based nano- or microstructured materials have been proposed and have received significant attention from the basic and applied chemistry research community over the last two decades [14–17]. These nanomaterials display unique features, including large surface areas and high physicochemical stability, compared to their parent compounds. Highly ordered and versatile geometric features render these materials suitable for applications in other fields, including chemical sensing [18], molecular recognition [19], catalysis [20], solar energy conversion and storage [21], and biomedical purposes [22]. Porphyrin molecules aggregate in solution and self-assemble to form larger stable molecules. Numerous intermolecular noncovalent interactions (e.g., hydrogen bonding interactions, π - π stacking interactions, ligand coordination, electrostatic interactions, van der Waals interactions, and hydrophobic and hydrophilic effects) facilitate the self-assembly of porphyrin molecules [23–27]. Therefore, the fabrication of well-defined prominent nanostructures from porphyrin compounds is a challenge. Various methods, including ionic assembly [28], metal-ligand coordination [29], re-precipitation [30], surfactant-assisted synthesis [31], and sonication [32], have been used for the construction of porphyrin-based self-assembled nanostructures. Ionic assemblies are extensively used for the construction of porphyrinoid-based nanosheets [33], nanotubes [28], nanospheres [34], nanofibers [35], nanorods [32], and nanocomposites [36] from various metalloporphyrins. Sn(IV) porphyrin complexes are suitable choices for the construction of functional porphyrin nanoaggregates because Sn(IV) centers are oxophilic and can readily form stable six-coordinate complexes with two *trans*-axial oxyanion ligands, such as alkoxides and carboxylates. In addition, these complexes have unique optical properties and are diamagnetic; therefore, structural information can be readily obtained using nuclear magnetic resonance (NMR) spectroscopy. They can also be used in the production of hydrogen gas [37–43].

Previously, we demonstrated the supramolecular ionic self-assemblies of highly-charged Sn(IV) porphyrin cations stabilized by counter anions [44,45]. In the present paper, the formation of Sn(IV) porphyrin-based ionic self-aggregated nanostructures has been described using Sn(IV) porphyrin complex **2** as the cation source (Chart 1). Precursor porphyrin **1** has also been used in competitive studies. The counter-anion source used was 1% aqueous solution of monoprotic acids (HCl, HNO_3 , and CF_3COOH), diprotic acids (H_2SO_4 and H_2CO_3), and a triprotic acid (H_3PO_4). In addition, the photocatalytic efficiency of these nanostructures was examined by monitoring the degradation of malachite green (MG) in an aqueous solution. MG is used as a natural green dye in textile industries, such as leather, wool, and silk [46]. MG, which possesses a cationic complex structure with a triphenylmethane core, is a carcinogenic, non-biodegradable, and toxic compound. Therefore, this dye can be used as a model pollutant to test the photocatalytic efficiency of the prepared catalysts in the laboratory [47,48].

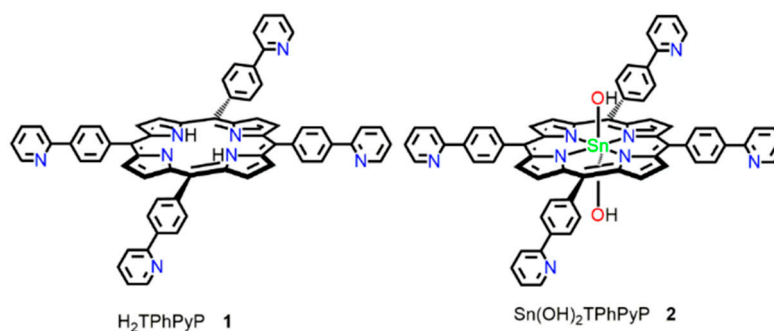
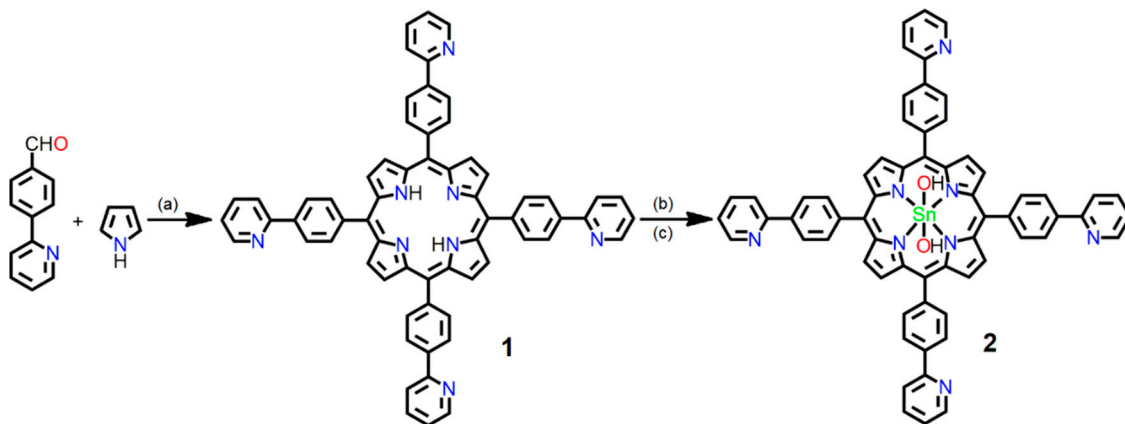


Chart 1. Chemical structures of compounds **1** and **2** used in this study.

2. Results and Discussions

2.1. Syntheses and Characterization

Scheme 1 illustrates the preparation of compounds **1** and **2**. First, H_2TPhPyP (**1**) was prepared from 4-(2-pyridyl)benzaldehyde and freshly distilled pyrrole in the presence of propionic acid under reflux conditions. Subsequently, compound **1** was treated with tin(II) chloride in the presence of pyridine, followed by hydrolysis, to form $\text{Sn(OH)}_2\text{TPhPyP}$ (**2**). Compounds **1** and **2** were fully characterized using various spectroscopic techniques, including elemental analysis, $^1\text{H-NMR}$ spectroscopy, ESI-MS, UV-vis spectroscopy, fluorescence spectroscopy, and Fourier transform infrared (FT-IR) spectroscopy.



Scheme 1. Synthesis of compounds **1** and **2**. Reaction conditions: (a) propionic acid, reflux, (b) $\text{SnCl}_2 \cdot 2\text{H}_2\text{O}$ /Pyridine, and (c) THF + Water/ K_2CO_3 .

$^1\text{H-NMR}$ spectra of compounds **1** and **2** were recorded in CDCl_3 and are shown in Figures S1 and S2. For compound **1**, the characteristic signal at 2.73 ppm corresponds to the NH protons of the pyrrole ring, while the protons in the pyridyl ring appear at 8.84, 8.04, 7.90, and 7.35 ppm. The phenyl protons of compound **1** are at 8.35 ppm, and the β -pyrrole protons appear at 8.94 ppm. Compound **2** exhibits a peak at 7.43 ppm corresponding to the axial Sn-OH protons. The pyridyl ring protons appear at 8.86, 8.07, 7.92, and 7.38 ppm. The β -pyrrole and phenyl protons of compound **2** appear at 9.23 and 8.45 ppm, respectively. ESI-MS spectra of compounds **1** and **2** are shown in Figures S3 and S4, respectively. Compound **1** has a molecular peak at 927.27 [**1** + H] $^+$, while **2** exhibits a peak at 1075.19 [**2** + H] $^+$. Furthermore, compound **2** has a low-intensity peak at 538.08, indicating the ion [**2** + 2H] $^{2+}$.

The UV-vis absorption spectra of compound **1** and its ionic complexes from various acids are shown in Figure 1. A sharp Soret band (419 nm) and four Q-bands (515, 551, 590, and 645 nm) were observed. After treatment with various acids to form the ionic complexes, the Soret band red-shifted (419 \rightarrow 422 nm for HNO_3 , CF_3COOH , and HCl ; 419 \rightarrow 442 nm for H_2SO_4), and an additional band at 443 nm in the case of HCl and CF_3COOH was observed. In the case of H_2CO_3 , the Soret band did not shift, but it was slightly broad compared with that of compound **1**. Conversely, Q-bands broadened with increasing intensity owing to

the formation of ionic complexes. The Soret band of the ionic complexes of compound **1** and H_3PO_4 showed a broad shift (half-width changed from 396 to 443 nm), and the Q bands red-shifted (515→524, 551→560, 590→596, and 645→654 nm). Similar trends were observed in the UV-vis absorption spectra of compound **2** and its ionic complexes with different acids (Figure 2). Compound **2** exhibited a typical sharp Soret band at 427 nm and Q-bands at 520, 560, and 601 nm. Blue shifts were observed in the Soret bands of all the ionic complexes of the acids: 427→420 nm for HCl , CF_3COOH , HNO_3 , and H_2SO_4 ; 427→416 nm for H_2CO_3 ; 427→418 nm for H_3PO_4 . The corresponding Q-bands also blue-shifted (551 and 592 nm). However, the Q bands also blue-shifted compared to those of compound **2** (566 and 609 nm).

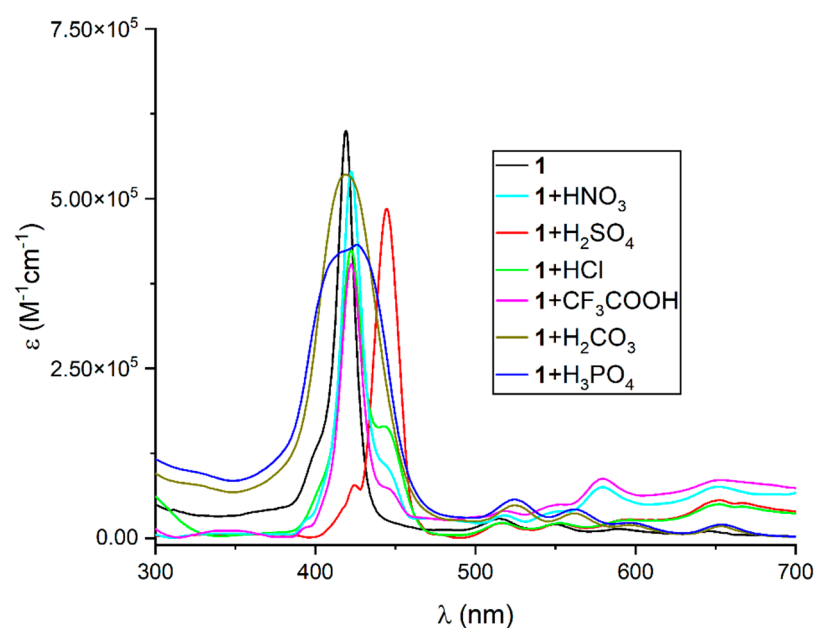


Figure 1. UV-visible spectra of compound **1** and its different ionic complexes in CHCl_3 .

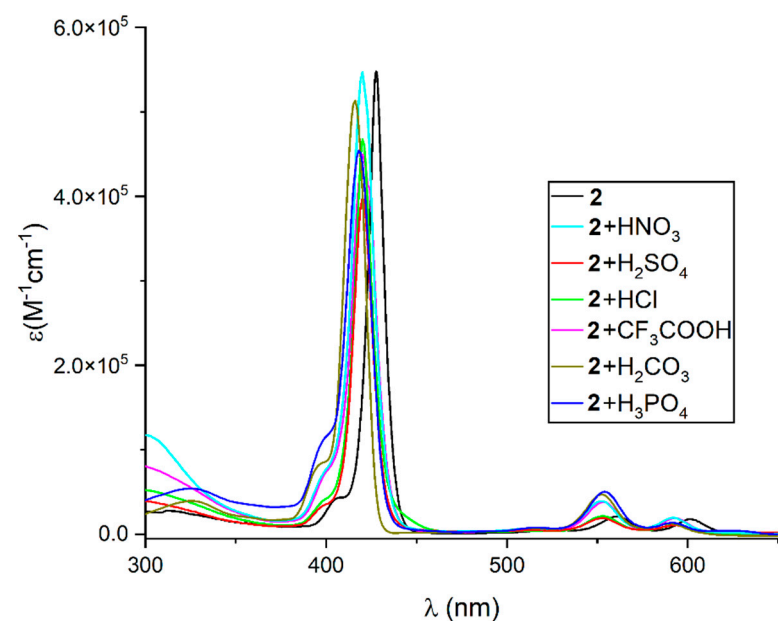


Figure 2. UV-visible spectra of compound **2** and its different ionic complexes in CHCl_3 .

The fluorescence spectra of compound **1** and its ionic complexes with various acids are shown in Figure 3. Compound **1** has a typical two-band emission spectrum (654 and 705 nm). After treatment with various acids to form ionic complexes, the intensities of

these two bands decreased without shifting. The fluorescence spectra of compound **2** and its ionic complexes are shown in Figure 4. Compound **2** has two emission bands (601 and 652 nm). Red shifts were observed for HCl and CF₃COOH ionic complexes (601→606 nm and 651→655 nm, respectively), while the emission intensity decreased considerably. In the case of H₂SO₄, HNO₃, H₂CO₃, and H₃PO₄ ionic complexes, these two bands did not shift, but their intensity decreased compared to that of compound **2**. The formation of the ionic complexes was further examined via FT-IR spectroscopy, as shown in Figures S5 and S6. Characteristic peaks were observed for NO₃[−] (1351 cm^{−1}), SO₄^{2−} (1110 cm^{−1}), CF₃COO[−] (1671 cm^{−1}), CO₃^{2−} (1410 cm^{−1}), and PO₄^{3−} (1010 cm^{−1}).

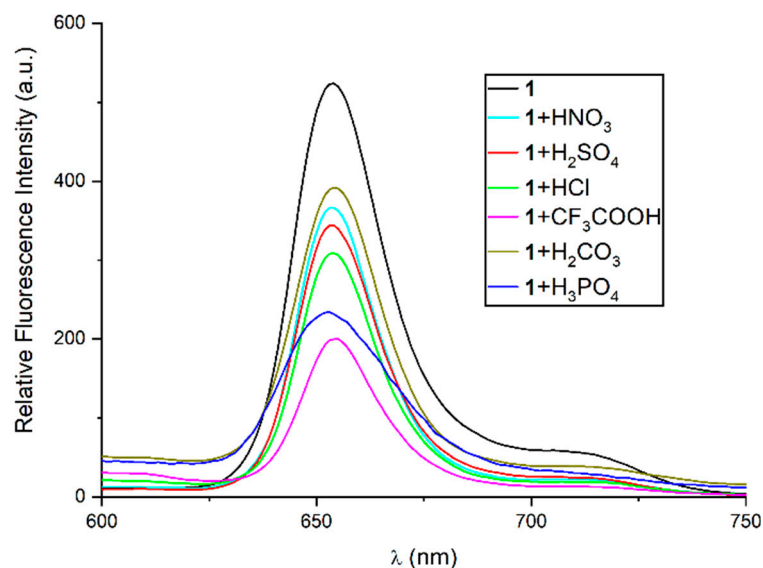


Figure 3. Fluorescence spectra of compound **1** and its different ionic complexes in CHCl₃. Optical density (OD) of the sample solution was fixed at 0.20.

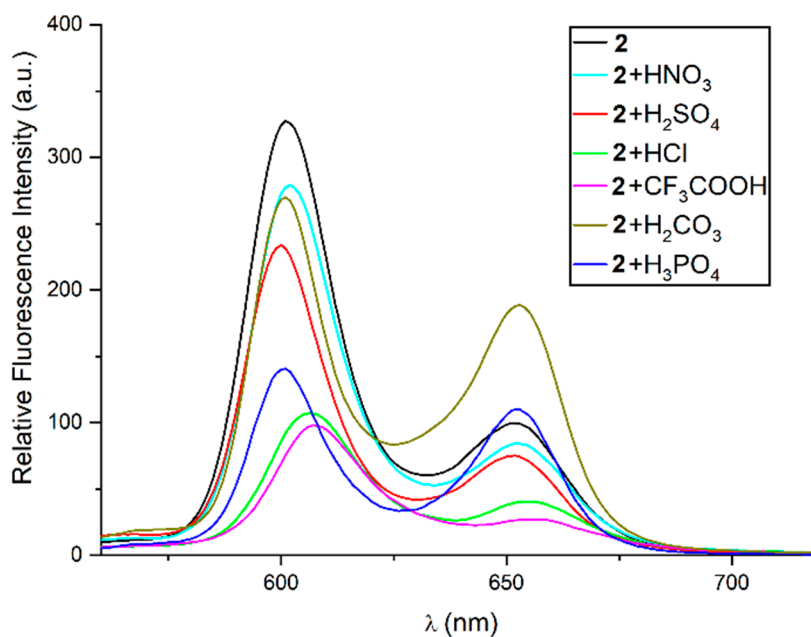


Figure 4. Fluorescence spectra of compound **2** and its different ionic complexes in CHCl₃. OD of the sample solution was fixed at 0.20.

2.2. Supramolecular Ionic Self-Assembly to Nanostructures

The self-assembly of compounds **1** and **2** and their ionic complexes were analyzed via field-emission scanning electron microscopy (FE-SEM). For sample preparation, each

complex was suspended in water at a fixed concentration ($c = 1 \text{ mM}$) and centrifuged at 13,500 rpm for 10 s. Thereafter, the solution was drop-casted onto the surface of a copper tape for deposition and dried in air, followed by Pt coating prior to the FE-SEM studies. The morphologies of the self-assembled nanostructures are shown in Figures 5 and 6. The average length of the spherical particles of compound 1 was from 110 to 200 nm (Figure 5a). In contrast, the average particle size of the truncated polyhedron of compound 2 was from 200 to 900 nm with a width of 100 nm (Figure 5b).

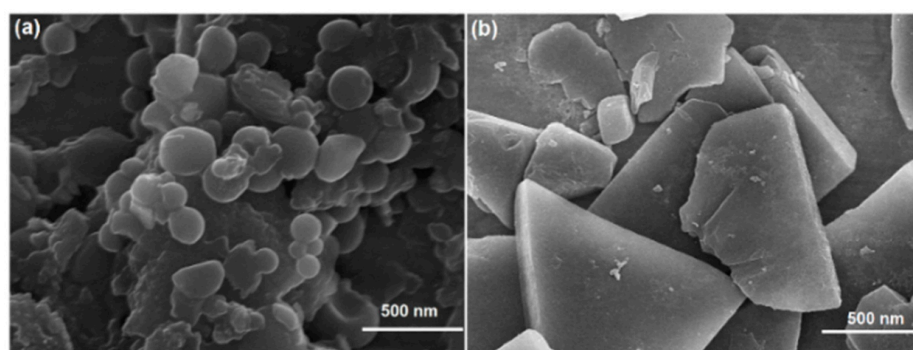


Figure 5. FE-SEM images for the morphology of compounds 1 (a) and 2 (b).

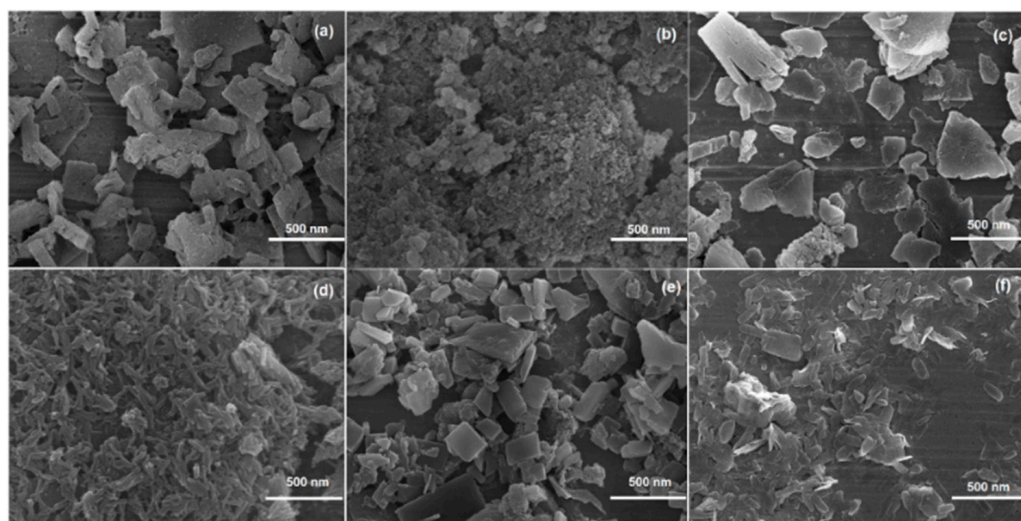


Figure 6. FE-SEM images depicting the morphology of ionic complexes derived from compound 1. (a) $1 + \text{H}_2\text{CO}_3$, (b) $1 + \text{HNO}_3$, (c) $1 + \text{H}_2\text{SO}_4$, (d) $1 + \text{HCl}$, (e) $1 + \text{CF}_3\text{COOH}$, and (f) $1 + \text{H}_3\text{PO}_4$.

After the formation of ionic complexes of compound 1 with various acids, its morphology changed significantly. In the case of ionic complexes derived from H_2CO_3 , the average particle size was from 250 to 350 nm, with a width of 50 nm (Figure 6a). The average particle size of the ionic complexes of compound 1 and HNO_3 was smaller (70–20 nm) (Figure 6b). In contrast, the particle size of the ionic complexes of compound 1 and H_2SO_4 was larger than that of compound 1, ranging from 250 to 600 nm (Figure 6c). Fused nanorods were observed in the ionic complexes of compound 1 and HCl , with the average length ranging from 160 to 40 nm (Figure 6d). The morphology of the ionic complexes of compound 1 and CF_3COOH exhibited rectangular-shaped structures ($210 \times 170 \times 80 \text{ nm}^3$) with several small particles (Figure 6e). Flake-shaped particles were observed in ionic complexes of compound 1 and H_3PO_4 (Figure 6f), with average particle size ranging from 200 to 260 nm in length and a width of 50 nm. From Figure 6, porphyrin ionic complexes of compound 1 and various acids self-assembled into nanostructures, and the morphology of these particles depends on the counter anions.

The morphologies of the self-assembled nanostructures obtained upon the formation of ionic complexes derived from compound **2** with various acids are shown in Figure 7. In the case of ionic complexes of H_2CO_3 , the average particle size of the sphere ranged from 70 to 140 nm (Figure 7a). Fused nanoflakes were observed in the ionic complex of compound **2** with HNO_3 (Figure 7b). A square-shaped morphology was observed in the complex of compound **2** with H_2SO_4 , with the average length of the fused square particles being 290 nm (Figure 7c). Fused rectangular-shaped structures ($240 \times 160 \times 55 \text{ nm}^3$) were observed for the ionic complexes of compound **2** and HCl (Figure 7d). The morphology of the ionic complexes of compound **2** and CF_3COOH was considerably different from that of compound **2** (Figure 7e) and demonstrated rectangular-shaped structures ($220 \times 90 \times 40 \text{ nm}^3$) along with fused spheres (average diameter of $\sim 120 \text{ nm}$). The morphologies of the ionic complexes of compound **2** and H_3PO_4 consisted of stone-like particles with lengths ranging from 90 to 300 nm and a width of 20 nm (Figure 7f). From Figure 7, it can be concluded that the counter anions affect the morphology of the ionic complexes derived from Sn(IV) porphyrin **2** with different acids.

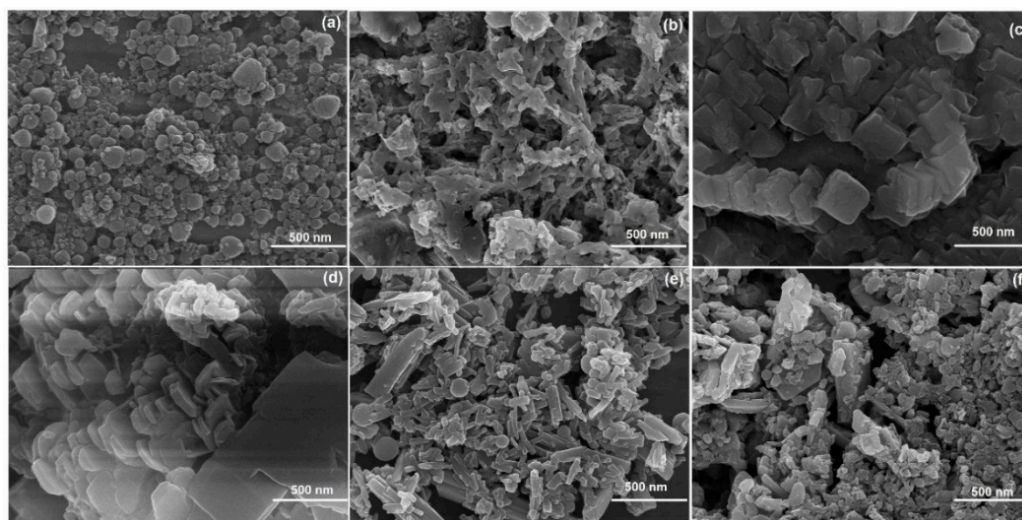


Figure 7. FE-SEM images illustrating the morphology of ionic complexes derived from compound **2**. (a) **2** + H_2CO_3 , (b) **2** + HNO_3 , (c) **2** + H_2SO_4 , (d) **2** + HCl , (e) **2** + CF_3COOH , and (f) **2** + H_3PO_4 .

2.3. Photocatalytic Performance for the Degradation of MG Dye

We have examined the photocatalytic activity of the photocatalysts developed in this study for the degradation of MG dye in aqueous solutions under visible-light irradiation. A negligible decay of the MG dye was observed in the absence of either a photocatalyst or visible light (Figure S7). ESI-MS spectra were recorded after 30 min in each photodegradation experiment. New small molecules from the degradation of the MG dye were formed, which was confirmed by the appearance of new peaks in the mass spectra. The time-dependent absorption spectra of MG in the presence of photocatalysts generated from compound **2** with H_3PO_4 under visible light irradiation are shown in Figure S8. From Figures 8 and 9, all the photocatalysts (generated from compounds **1** and **2** with various acids) were effective for the photodegradation of MG, and their photocatalytic performance depended on the morphology of the nanoaggregates. The degradation rates of MG dye in the presence of a photocatalyst can be determined from its degradation efficiency, $(C_0 - C)/C_0$, where C_0 is the initial concentration of MG, and C is the concentration at time t . The observed degradation rates of MG were 50% for compound **1** and 53, 60, 66, 73, 86, and 90% for the photocatalysts derived from compound **1** with H_2CO_3 , HNO_3 , H_2SO_4 , HCl , CF_3COOH , and H_3PO_4 , respectively (Figure 8).

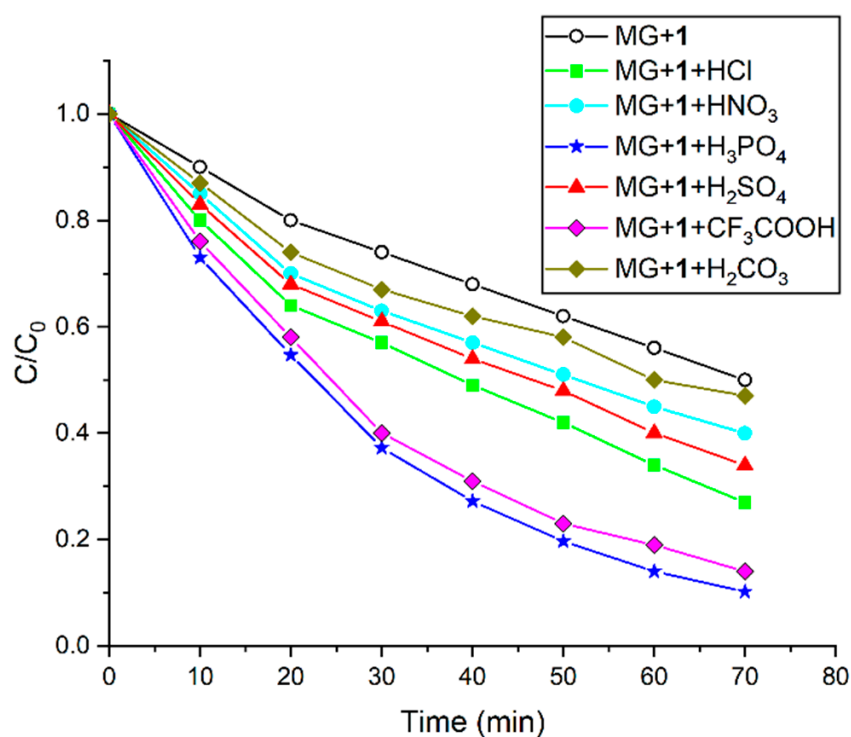


Figure 8. Photocatalytic degradation of MG dye in aqueous solution (pH 7, temperature 298 K) under visible light irradiation by photocatalysts generated from compound 1 with various acids.

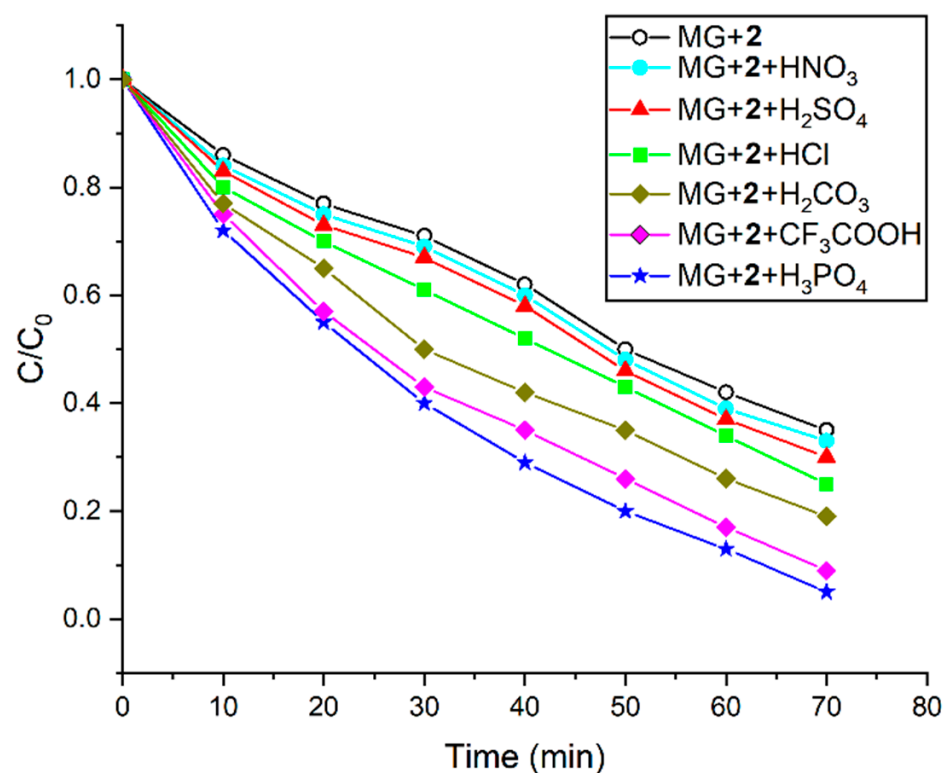


Figure 9. Photocatalytic degradation of the MG dye in aqueous solution (pH 7, temperature 298 K) under visible light irradiation by photocatalysts generated from compound 2 with various acids.

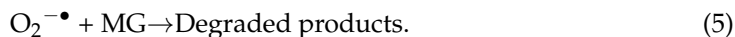
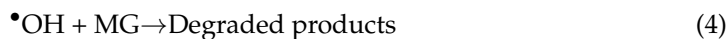
In contrast, the observed degradation rate of MG was 65% for compound 2 and 67, 70, 75, 80, 91, and 95% for the photocatalysts derived from compound 2 with HNO₃, H₂SO₄, HCl, H₂CO₃, CF₃COOH, and H₃PO₄, respectively (Figure 9). From the above observation,

it was clear that the photocatalysts derived from **1** and **2** with H_3PO_4 showed the optimum performance towards the decay of MG dye. To further elucidate the reaction kinetics for the degradation of the MG dye, the pseudo-first-order rate equation was used for the photocatalytic degradation experiments. The equation was expressed as $\ln(C_0/C) = kt$, where C_0 is the initial concentration of dye, C represents dye concentration at irradiation time t , and k denotes the pseudo-first-order rate constant. Using the data displayed in Figures 8 and 9, the reaction kinetics of the MG dye degradation are presented in Figures S9 and S10. The first-order rate constant for the degradation of MG by compound **1** was 0.009 min^{-1} , and the other rate constants were 0.011, 0.013, 0.015, 0.017, 0.028, and 0.032 min^{-1} for the photocatalysts derived from compound **1** with H_2CO_3 , HNO_3 , H_2SO_4 , HCl , CF_3COOH , and H_3PO_4 , respectively (Figure S9).

Similarly, the first-order rate constant for the degradation of MG by compound **2** was 0.014 min^{-1} and the other rate constants were 0.015, 0.016, 0.018, 0.022, 0.032, and 0.039 min^{-1} for the photocatalysts derived from compound **2** with HNO_3 , H_2SO_4 , HCl , H_2CO_3 , CF_3COOH , and H_3PO_4 , respectively (Figure S10). Previously, various investigations concerning the MG dye degradation have been reported in the literature. Our observed rate constants were comparable to or even better than those reported for other photocatalysts such as TiO_2 (0.0064 to 0.140 min^{-1}) [47], Zn(II)porphyrin with H_2O_2 (0.0042 to 0.0054 min^{-1}) [48], Au-Ag/TiO_2 (0.00987 to 0.2595 min^{-1}) [49], and CuFe_2O_4 (0.0142 min^{-1}) [50]. In addition, the recovery of the photocatalysts from the reaction vessel was easily handled by a continuous filtration-wash-dry procedure. The efficiency of the photocatalyst remained unchanged after recovery, and it showed excellent recyclability for the degradation of MG dye (Figure S11). It should be noted that the efficiency of photocatalyst (derived from **2** with H_3PO_4) remained almost intact even after 10 consecutive cycles. As depicted in Figure S11, 95% MG was degraded within 70 min for the first run, and the photocatalytic performance slightly decreased, marked by 91% MG degradation, after 10 consecutive cycles. The morphology of the catalysts remained intact after their use in the degradation experiment, as confirmed by the FE-SEM image of the photocatalyst derived from compound **2** with H_3PO_4 (Figure S12).

To examine the effect of dye/catalyst ratio on the performance of the photocatalysts, different concentrations of the MG dye aqueous solution (5, 10, 15, 20, 30, and 40 mg L^{-1}) with a fixed amount of catalyst (5 mg each time) were used for each time. From Figure S13, it was revealed that the degradation rate gradually decreased as the concentration of MG dye increased. The effect of the temperature and the pH on the degradation of MG dye has been also examined. From the Figure S14, it was observed that degradation efficiency increased with increasing temperature. As shown in Figure S15, the pH of the MG dye solution affected the degradation rate. The rate of degradation increased from pH 2 to pH 7, and then decreased up to pH 11.

Several possible mechanisms for the photodegradation of pollutant dyes in aqueous solutions using porphyrin-based photocatalysts have been reported [11,15–17]. The mechanism consists of five steps for porphyrin-based nanomaterials (**P**). When the photocatalyst absorbs visible-light irradiation, electrons in the valence band (VB) are excited to the conduction band (CB). The electron-hole pairs (e^-/h^+) are formed through this process at the surface of the photocatalyst (step 1). Intermolecular π - π interactions stabilized the electronic delocalization over the nanomaterials and minimize the recombination energy of the excited electrons. Next, the photogenerated holes (h^+) react with H_2O to produce reactive species of hydroxyl radicals ($\bullet\text{OH}$). On the other hand, the reaction of the electrons with the dissolved O_2 generate superoxide radical anions ($\text{O}_2^{\bullet-}$) (steps 2 and 3). Then these reactive species (superoxide radical anions and hydroxyl radicals) react with the MG dye and mineralized it into low molecular compounds (steps 4 and 5).



Reactive species involved in the photocatalytic degradation of the MG dye by the photocatalyst generated from compound **2** and H_3PO_4 were identified via radical trapping analysis [51]. To investigate the effect of different reactive species on the photodegradation of the MG dye, *tert*-butyl alcohol ($tBuOH$) and *para*-benzoquinone (BQ) were used to capture $\bullet OH$ and $O_2^{\bullet -}$, respectively (Figure S16). From Figure S16, the degradation rate was affected by the presence of $tBuOH$ as well as BQ, suggesting that hydroxyl radicals and superoxide radicals are the major reactive species that contribute to the catalytic oxidation of the MG dye. For further details on the detection of all intermediate species involved in the dye degradation process (all oxygen species, such as 1O_2 and 3O_2 , $\bullet OH$, or $O_2^{\bullet -}$), readers can refer to our previous reports [11,15–17].

In order to examine the adsorption properties of the photocatalysts towards the MG dye, the Brunauer–Emmett–Teller (BET) surface area of the photocatalysts (derived from **1** and **2** with H_3PO_4) was measured. Figure S17 presents the N_2 adsorption-desorption isotherms of the photocatalysts (derived from **1** and **2** with H_3PO_4). Each photocatalyst exhibited a low surface area, for example the BET surface area of the best performing photocatalysts (derived from **1** and **2** with H_3PO_4) were estimated to be $4.5 \text{ m}^2/\text{g}$ and $12.7 \text{ m}^2/\text{g}$, respectively. As shown in Figure S18, it took about 30 min to reach the absorption-desorption equilibrium, 2% and 5% of MG dye were adsorbed by the photocatalysts derived from **1** and **2** with H_3PO_4 , respectively. Lower adsorption of dye on the surface of photocatalysts have some advantages as the bare active sites are readily available for photodegradation. However, the absorption of dye on the surface of photocatalyst not only depends on the surface area of the catalyst but also the interaction of dye with active sites of the photocatalysts and various interaction at the junction of solid-liquid interface.

The reaction mixture was analyzed after 30 min irradiation of visible light using ESI-MS (Figure S19) to study the details of the degradation pathway of the MG dye. New peaks appeared in the mass spectra imply that the MG dye was degraded into new small molecules [52,53]. By analyzing mass spectral data in Figure S19, possible intermediates for the degradation of the MG dye are given in Figure 10. The degradation of the MG dye can occur in two different ways. First, the reaction of the hydroxyl radical with the MG cation forms a carbinol intermediate with m/z 347.2. This intermediate is further fragmented into smaller intermediates with m/z 269.1, 226.1, and 199.0 and hydroquinone (m/z 111.0). Second, the *N*-demethylation of the MG cation forms an intermediate (m/z 273.1), followed by the formation of a hydroxyl radical species (m/z 291.1) and finally fragmentation into a molecule with m/z 213.1. Further successive breakdown leads to the formation of hydroquinone. Hydroquinone is further fragmented into benzoquinone and then to maleic acid. Finally, all intermediate molecules were further fragmented and mineralized into CO_2 and H_2O . Moreover, the total organic carbon (TOC) value was measured to evaluate the removal of the MG dye by photocatalysts [54]. The TOC removal percentage achieved using the photocatalyst generated from compound **2** and H_3PO_4 was only 75%.

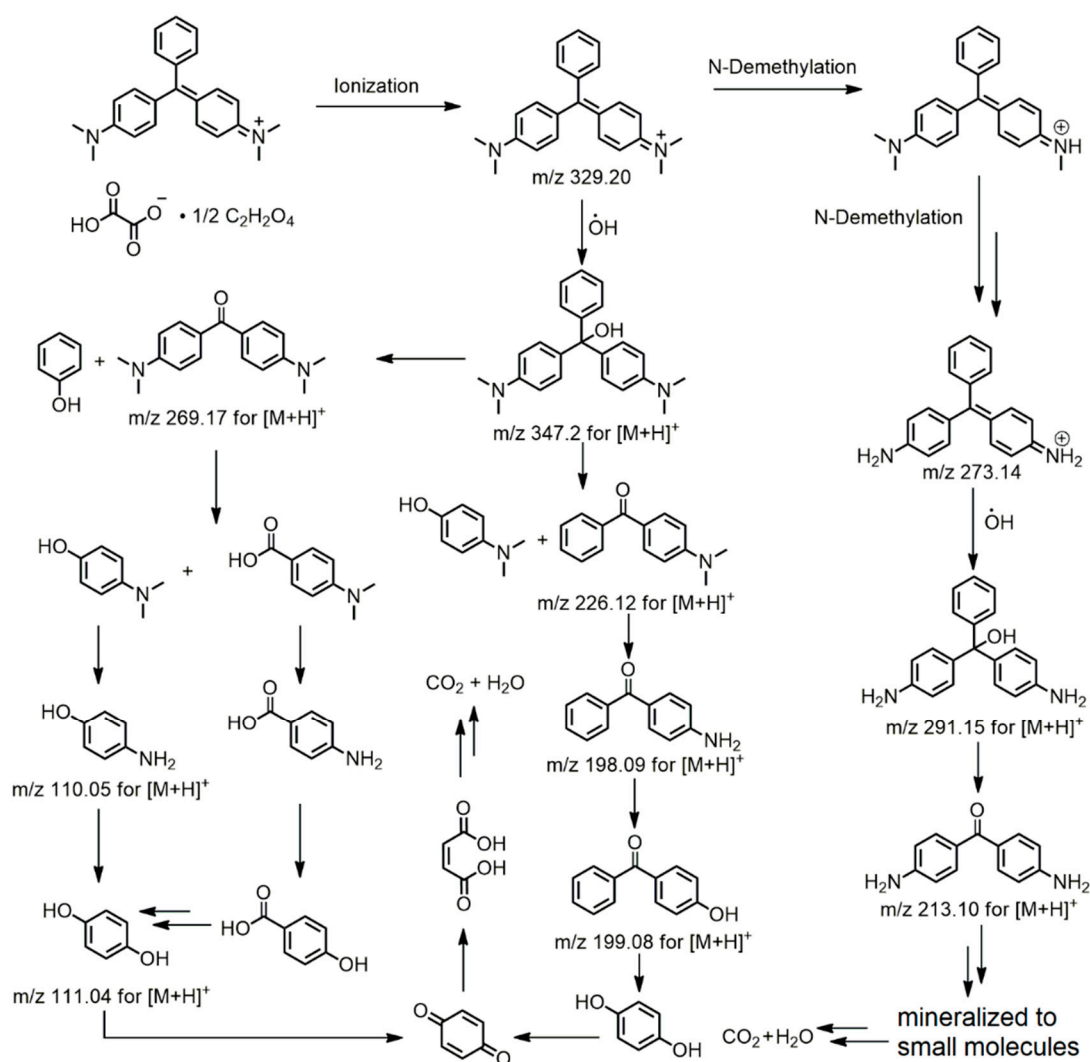


Figure 10. Possible intermediates of the reaction between MG and the photocatalyst under visible light irradiation in aqueous solution.

3. Materials and Methods

All chemicals were purchased from Tokyo Chemical Industry Co. LTD. (Tokyo, Japan) and used without further purification. Elemental analysis was conducted using an EA 1110 Fisons analyzer (Used Lab Machines Limited, London, UK). ^1H -NMR spectra were recorded on a Bruker BIOSPIN/AVANCE III 400 spectrometer at 293 K (Bruker BioSpin GmbH, Silberstreifen, Rheinstetten, Germany). ESI-MS spectra were recorded using a Thermo Finnigan linear ion trap quadrupole mass spectrometer (Thermo Fisher Scientific, Waltham, MA, USA). Steady-state UV-vis and fluorescence spectra were recorded on a Shimadzu UV-3600 spectrophotometer and a Shimadzu RF-5301PC fluorescence spectrophotometer, respectively. FT-IR spectra were measured using a Shimadzu FTIR-8400S spectrophotometer (Shimadzu, Tokyo, Japan). FE-SEM images were obtained using a MAIA III system (TESCAN, Brno, Czech Republic). The Brunauer–Emmett–Teller (BET) surface area using N_2 adsorption isotherms at 77 K was measured with an analyzer (BELSORP-mini volumetric adsorption equipment). The total organic carbon (TOC) values of the degradation of MG dye were examined with a JEOL JEM-3010 total organic carbon analyzer to calculate the extent of mineralization.

3.1. Synthesis of 5,10,15,20-Tetrakis [4-(2-Pyridyl)phenyl]porphyrin $H_2TPhPyP$ (1)

Freshly distilled pyrrole (0.38 mL, 5.5 mmol) was added dropwise to a solution of 4-(2-pyridyl)benzaldehyde (1.00 g, 5.5 mmol) in propionic acid (200 mL) under reflux. After 3 h, the solvent was evaporated to dryness under vacuum to obtain an oily residue. Thereafter, the oily residue was neutralized with trimethylamine and dissolved in a minimum amount of *N,N*-dimethylformamide. The reaction mixture was stored in a refrigerator overnight. The resulting solid was filtered, washed with hot water, and dried. The crude product was purified using column chromatography (SiO_2 , eluent: $CH_2Cl_2/MeOH = 90:10$) to afford 5,10,15,20-tetrakis [4-(2-pyridyl)phenyl]porphyrin **1**. The crude product was recrystallized from CH_2Cl_2/n -hexane to obtain a violet-purple crystalline powder. Yield: 0.127 g (10%). Anal calculated for $C_{64}H_{42}N_8$: C, 83.27; H, 4.59; N, 12.14. Found: C, 83.05; H, 4.67; N, 12.28. 1H -NMR (400 MHz, $CDCl_3$, ppm): δ −2.73 (s, 2H, NH), 7.35 (m, 4H, H4-Py), 7.90 (m, 4H, H3-Py), 8.04 (d, $J = 7.8$ Hz, 4H, H5-Py), 8.35 (dd, 16H, $H_{o,m}$ -Ph), 8.84 (d, $J = 4.8$ Hz, 4H, H2-Py), 8.94 (s, 8H, β -pyrrole). UV-visible ($CHCl_3$): λ_{nm} (log ϵ), 419 (5.78), 515 (4.47), 551 (4.33), 590 (4.10), 645 (4.04). Emission ($CHCl_3$, λ_{nm}): 654 and 705.

3.2. Synthesis of Trans-dihydroxo-[5,10,15,20-tetrakis(4-(2-pyridyl)phenyl)porphyrinato]tin(IV) $Sn(OH)_2TPhPyP$ (2)

$H_2TPhPyP$ (0.092 g, 0.1 mmol) was dissolved in pyridine (50 mL), and $SnCl_2 \cdot 2H_2O$ (0.22 g, 0.85 mmol) was added to the solution and refluxed for 15 h. Subsequently, pyridine was removed under vacuum, and the residue was dissolved in $CHCl_3$ and filtered through a celite pad to remove excess $SnCl_2$. The filtrate was evaporated, and the crude was re-dissolved in a solvent mixture (50 mL) consisting of tetrahydrofuran (THF; 40 mL) and H_2O (10 mL). K_2CO_3 (0.33 g, 1.45 mmol) was added to the reaction mixture, and it was refluxed for 10 h. THF was removed under reduced pressure conditions, and the mixture was cooled to 5 °C to precipitate the product. The solid compound was then filtered and dried in an oven. Recrystallization ($CHCl_3/CH_3CN$) afforded a reddish compound **2**. Yield 90 mg (84%). Anal calculated for $C_{64}H_{42}N_8O_2Sn$: C, 71.59; H, 3.94; N, 10.44; R, 14.03. Found: C, 71.42; H, 4.11; N, 10.37; R, 14.10. 1H -NMR (400 MHz, $CDCl_3$, ppm): δ −7.38 (m, 4H, H4-Py), 7.43 (s, 2H, Sn-OH), 7.92 (m, 4H, H3-Py), 8.07 (d, $J = 7.7$ Hz, 4H, H5-Py), 8.45 (m, 16H, $H_{o,m}$ -Ph), 8.86 (d, $J = 4.7$ Hz, 4H, H2-Py), 9.23 (m, 8H, β -pyrrole). UV-visible ($CHCl_3$): λ_{nm} (log ϵ), 427 (5.50), 520 (3.70), 560 (4.35), 601 (4.25). Emission ($CHCl_3$, λ_{nm}): 601 and 652.

3.3. Synthesis of the Ionic Complexes of $H_2TPhPyP$ (1) and $Sn(OH)_2TPhPyP$ (2) Using Various Acids

Ten milligrams of each of the porphyrin compounds (**1** and **2**) were dissolved in a 1% aqueous solution (5 mL) of each of the following acids—HCl, HNO_3 , CF_3COOH , H_2SO_4 , H_2CO_3 , and H_3PO_4 , and acetone (20 mL) was layered over for slow diffusion for 7 d. Subsequently, the crystalline materials were filtered, washed with water, and air-dried.

3.4. Photocatalytic Investigation

The photocatalytic efficiency of the self-assembled ionic nanostructures was studied by monitoring the degradation of MG dye in an aqueous solution by the catalysts, using malachite oxalate green salt as the source of MG. In a typical procedure, 5 mg of the photocatalyst was added to 150 mL of aqueous MG solution (20 mg L^{-1} , distilled water at pH 7.0) with stirring. The mixture was then placed in the dark for 30 min to attain an adsorption-desorption equilibrium. The irradiation process was conducted using a 150 W xenon arc lamp with a UV cut-off filter (ABET technologies, Old gate lane Milford, Milford, CT, USA) at room temperature. At specified intervals, 3 mL of the suspension was centrifuged to remove the photocatalyst. Subsequently, the solution was analyzed by recording absorption variations in the UV-Vis spectra at 617 nm to determine the concentration of MG.

4. Conclusions

In this study, various porphyrin-based ionic complexes were prepared through the reaction of two porphyrin precursors, compounds **1** and **2**, with various acids (HCl, HNO₃, CF₃COOH, H₂SO₄, H₂CO₃, and H₃PO₄). Depending on the counter anion [55,56], these complexes readily assembled into different nanostructures, based on the electronic interaction of cations of compounds **1** or **2** with different counter anions. These nanostructures can be further stabilized through π - π stacking interactions between the phenyl-extended porphyrin rings. Furthermore, the morphology-dependent photocatalytic degradation of MG dye in aqueous solution under visible light irradiation for 70 min was observed for all the ionic complexes, with efficiencies ranging from 50% to 95%. Therefore, counter anions can affect the morphology as well as the optical properties of porphyrin-based species. In addition, the aggregates are good photocatalysts for the treatment of wastewater.

Supplementary Materials: The following supporting information can be downloaded at <https://www.mdpi.com/article/10.3390/catal12070799/s1>, ¹H-NMR spectra, mass spectra, and results of the photocatalytic degradation of MG are shown in Figures S1–S19. Figure S1: ¹H-NMR spectrum of compound **1**; Figure S2: ¹H-NMR spectrum of compound **2**; Figure S3: ESI-MS spectrum of compound **1**; Figure S4: ESI-MS spectrum of compound **2**; Figure S5: FT-IR spectra of compound **1** and its ionic complexes; Figure S6: FT-IR spectra of compound **2** and its ionic complexes; Figure S7: UV-vis spectroscopic observation of the photocatalytic degradation of MG dye in aqueous solution under visible light irradiation by photocatalyst **1** and **2**; Figure S8: Absorption spectral change of MG dye for the photocatalytic degradation by photocatalyst generated from **2** and H₃PO₄ in aqueous solution under visible light irradiation; Figure S9: Kinetics for the photocatalytic degradation of MG under visible light irradiation by photocatalyst generated from **1** and various acids; Figure S10: Kinetics for the photocatalytic degradation of MG under visible light irradiation by photocatalyst generated from **2** and various acids; Figure S11: Recyclability of the photocatalyst generated from **2** and H₃PO₄ towards the degradation of MG dye; Figure S12: FE-SEM images of photocatalyst generated from **2** and H₃PO₄ (after and before the degradation of MG dye); Figure S13: Effect of initial concentration of MG on the degradation by the photocatalyst (5 mg) generated from **2** and H₃PO₄; Figure S14: Effect of temperature on the MG degradation by the photocatalyst generated from **2** and H₃PO₄; Figure S15: Effect of pH of the solution on the MG degradation by the photocatalyst generated from **2** and H₃PO₄; Figure S16: Photocatalytic degradation of MG dye in aqueous solution by the photocatalyst generated from **2** and H₃PO₄ with the addition of different scavengers under visible light irradiation; Figure S17: N₂ adsorption-desorption isotherms at 77 K for the photocatalysts derived from **1** and **2** with H₃PO₄; Figure S18: Adsorption of MG dye for the photocatalysts derived from **1** and **2** with H₃PO₄; Figure S19: ESI-MS spectrum (positive ion mode) of the reaction mixture of MG with the photocatalyst generated from **2** and H₃PO₄ after 30 min of visible light irradiation.

Author Contributions: Investigation, methodology, data curation, visualization, formal analysis, validation, software, and writing, N.K.S.; conceptualization, review, editing, supervision, project administration, and funding acquisition, H.-J.K. All authors read and agreed to the published version of the manuscript.

Funding: National Research Foundation of Korea (NRF) grant (Grant No. 2022R1F1A1074420).

Data Availability Statement: Data are available in the article and Supplementary Materials.

Acknowledgments: This study was supported by a National Research Foundation of Korea (NRF) grant (Grant No. 2022R1F1A1074420) funded by the Korean Government (MSIT).

Conflicts of Interest: The authors declare no conflict of interest.

References

- Schwarzenbach, R.P.; Egli, T.; Hofstetter, T.; Von Gunten, U.; Wehrli, B. Global Water Pollution and Human Health. *Annu. Rev. Environ. Resour.* **2010**, *35*, 109–136. [CrossRef]
- Hunt, C.F.; Voulvoulis, N. Chemical pollution of the aquatic environment and health. In *Environmental Pollutant Exposures and Public Health*; The Royal Society of Chemistry: London, UK, 2021; pp. 39–69.
- Ain, Q.U.; Rasheed, U.; Yaseen, M.; Zhang, H.; Tong, Z. Superior dye degradation and adsorption capability of polydopamine modified Fe₃O₄-pillared bentonite composite. *J. Hazard. Mater.* **2020**, *397*, 122758. [CrossRef] [PubMed]

4. Thamaraiselvan, C.; Noel, M. Membrane processes for dye wastewater treatment; recent progress in fouling control. *Crit. Rev. Environ. Sci. Technol.* **2015**, *45*, 1007–1040. [[CrossRef](#)]
5. Wawrzkievicz, M. Anion-Exchange Resins for C.I. Direct Blue 71 Removal from Aqueous Solutions and Wastewaters: Effects of Basicity and Matrix Composition and Structure. *Ind. Eng. Chem. Res.* **2014**, *53*, 11838–11849. [[CrossRef](#)]
6. Balcha, A.; Yadav, O.P.; Dey, T. Photocatalytic degradation of methylene blue dye by zinc oxide nanoparticles obtained from precipitation and sol-gel methods. *Environ. Sci. Pollut. Res.* **2016**, *23*, 25485–25493. [[CrossRef](#)]
7. Łuba, M.; Mikołajczyk, T.; Pierożyński, B.; Smoczyński, L.; Wojtacha, P.; Kuczyński, M. Electrochemical Degradation of Industrial Dyes in Wastewater through the Dissolution of Aluminum Sacrificial Anode of Cu/Al Macro-Corrosion Galvanic Cell. *Molecules* **2020**, *25*, 4108. [[CrossRef](#)] [[PubMed](#)]
8. Xu, J.; Gao, Q.Z.; Wang, Z.P.; Zhu, Y. An all-organic 0D/2D supramolecular porphyrin/g-C₃N₄ heterojunction assembled via π - π interaction for efficient visible photocatalytic oxidation. *Appl. Catal. B Environ.* **2021**, *291*, 120059. [[CrossRef](#)]
9. Khin, M.; Nair, A.; Babu, V.; Murugan, R.; Ramakrishna, S. A review on nano-materials for environmental remediation. *Energy Environ. Sci.* **2012**, *5*, 8075–8109. [[CrossRef](#)]
10. Wang, C.C.; Li, J.R.; Lv, X.L.; Zhang, Y.Q.; Guo, G. Photocatalytic Organic Pollutants Degradation in Metal-Organic Frameworks. *Energy Environ. Sci.* **2014**, *7*, 2831–2867. [[CrossRef](#)]
11. Shee, N.K.; Jo, H.J.; Kim, H.-J. Coordination framework materials fabricated by the self-assembly of Sn(IV) porphyrins with Ag(I) ions for the photocatalytic degradation of organic dyes in wastewater. *Inorg. Chem. Front.* **2022**, *9*, 1270–1280. [[CrossRef](#)]
12. O'Regan, B.; Grätzel, M. A low-cost, high-efficiency solar cell based on dye-sensitized colloidal TiO₂ films. *Nature* **1991**, *353*, 737–740. [[CrossRef](#)]
13. Linsebigler, A.L.; Lu, G.Q.; Yates, J.T. Photocatalysis on TiO₂ surfaces: Principles, mechanisms, and selected results. *Chem. Rev.* **1995**, *95*, 735–758. [[CrossRef](#)]
14. Chen, Y.; Li, A.; Huang, Z.-H.; Wang, L.-N.; Kang, F. Porphyrin-Based Nanostructures for Photocatalytic Applications. *Nanomaterials* **2016**, *6*, 51. [[CrossRef](#)] [[PubMed](#)]
15. Shee, N.K.; Kim, M.K.; Kim, H.-J. Supramolecular Porphyrin Nanostructures Based on Coordination-Driven Self-Assembly and Their Visible Light Catalytic Degradation of Methylene Blue Dye. *Nanomaterials* **2020**, *10*, 2314. [[CrossRef](#)] [[PubMed](#)]
16. Shee, N.K.; Kim, H.-J. Self-Assembled Nanomaterials Based on Complementary Sn(IV) and Zn(II)-Porphyrins, and Their Photocatalytic Degradation for Rhodamine B Dye. *Molecules* **2021**, *26*, 3598. [[CrossRef](#)] [[PubMed](#)]
17. Shee, N.K.; Kim, H.-J. Three Isomeric Zn(II)-Sn(IV)-Zn(II) Porphyrin-Triad-Based Supramolecular Nanoarchitectures for the Morphology-Dependent Photocatalytic Degradation of Methyl Orange. *ACS Omega* **2022**, *7*, 9775–9784. [[CrossRef](#)]
18. Magna, G.; Mandoj, F.; Stefanelli, M.; Pomarico, G.; Monti, D.; Di Natale, C.; Paolesse, R.; Nardis, S. Recent Advances in Chemical Sensors Using Porphyrin-Carbon Nanostructure Hybrid Materials. *Nanomaterials* **2021**, *11*, 997. [[CrossRef](#)]
19. Farinone, M.; Urbńska, K.; Pawlicki, M. BODIPY- and Porphyrin-Based Sensors for Recognition of Amino Acids and Their Derivatives. *Molecules* **2020**, *25*, 4523. [[CrossRef](#)]
20. Nikolaou, V.; Charalambidis, G.; Coutsolelos, A.G. Photocatalytic hydrogen production of porphyrin nanostructures: Spheres vs. fibrils, a case study. *Chem. Commun.* **2021**, *57*, 4055–4058. [[CrossRef](#)]
21. Hasobe, T. Porphyrin-Based Supramolecular Nanoarchitectures for Solar Energy Conversion. *J. Phys. Chem. Lett.* **2013**, *4*, 1771–1780. [[CrossRef](#)]
22. Grigore, M.E.; Ion, R.-M.; Iancu, L. Tailored porphyrin-gold nanoparticles for biomedical applications. *J. Porphyr. Phthalocyanines* **2019**, *23*, 766–780. [[CrossRef](#)]
23. Lehn, J.-M. Perspectives in Supramolecular Chemistry—From Molecular Recognition towards Molecular Information Processing and Self-Organization. *Angew. Chem. Int. Ed. Engl.* **1990**, *29*, 1304–1319. [[CrossRef](#)]
24. Drain, C.M.; Varotto, A.; Radivojevic, I. Self-Organized Porphyrinic Materials. *Chem. Rev.* **2009**, *109*, 1630–1658. [[CrossRef](#)] [[PubMed](#)]
25. Beletskaya, I.; Tyurin, V.S.; Tsivadze, A.Y.; Guillard, R.; Stern, C. Supramolecular chemistry of metalloporphyrins. *Chem. Rev.* **2009**, *109*, 1659–1713. [[CrossRef](#)] [[PubMed](#)]
26. Shao, S.; Rajendiran, V.; Lovell, J.F. Metalloporphyrin nanoparticles: Coordinating diverse theranostic functions. *Coord. Chem. Rev.* **2019**, *379*, 99–120. [[CrossRef](#)]
27. Shee, N.K.; Seo, J.-W.; Kim, H.-J. Spectrophotometric Study of Bridging N-Donor Ligand-Induced Supramolecular Assembly of Conjugated Zn-Trisporphyrin with a Triphenylamine Core. *Molecules* **2021**, *26*, 4771. [[CrossRef](#)]
28. Wang, Z.; Medforth, C.J.; Shelnutt, J.A. Porphyrin Nanotubes by Ionic Self-Assembly. *J. Am. Chem. Soc.* **2004**, *126*, 15954–15955. [[CrossRef](#)]
29. Maeda, H.; Hasegawa, M.; Hashimoto, T.; Kakimoto, T.; Nishio, S.; Nakanishi, T. Nanoscale Spherical Architectures Fabricated by Metal Coordination of Multiple Dipyrin Moieties. *J. Am. Chem. Soc.* **2006**, *128*, 10024–10025. [[CrossRef](#)]
30. Gong, X.; Milic, T.; Xu, C.; Batteas, J.D.; Drain, C.M. Preparation and Characterization of Porphyrin Nanoparticles. *J. Am. Chem. Soc.* **2002**, *124*, 14290–14291. [[CrossRef](#)]
31. Zhang, C.; Chen, P.; Dong, H.; Zhen, Y.; Liu, M.; Hu, W. Porphyrin Supramolecular 1D Structures via Surfactant-Assisted Self-Assembly. *Adv. Mater.* **2015**, *27*, 5379–5387. [[CrossRef](#)]
32. Hasobe, T.; Oki, H.; Sandanayakaa, A.S.D.; Murata, H. Sonication-assisted supramolecular nanorods of meso-diaryl-substituted porphyrins. *Chem. Commun.* **2008**, 724–726. [[CrossRef](#)] [[PubMed](#)]

33. Tian, Y.; Beavers, C.M.; Busani, T.; Martin, K.E.; Jacobsen, J.L.; Mercado, B.Q.; Swartzentruber, B.S.; van Swol, F.; Medforth, C.J.; Shelnutt, J.A. Binary ionic porphyrin nanosheets: Electronic and light-harvesting properties regulated by crystal structure. *Nanoscale* **2012**, *4*, 1695–1700. [[CrossRef](#)] [[PubMed](#)]
34. Bera, K.; Mondal, A.; Pal, U.; Maiti, N.C. Porphyrin-Armored Gold Nanospheres Modulate the Secondary Structure of α -Synuclein and Arrest Its Fibrillation. *J. Phys. Chem. C* **2020**, *124*, 6418–6434. [[CrossRef](#)]
35. Jang, J.H.; Jeon, K.-S.; Oh, S.; Kim, H.-J.; Asahi, T.; Masuhara, H.; Yoon, M. Synthesis of Sn-Porphyrin-Intercalated Trititanate Nanofibers: Optoelectronic Properties and Photocatalytic Activities. *Chem. Mater.* **2007**, *19*, 1984–1991. [[CrossRef](#)]
36. Tian, Y.; Busani, T.; Uyeda, G.H.; Martin, K.E.; van Swol, F.; Medforth, C.J.; Montan, G.A.; Shelnutt, J.A. Hierarchical cooperative binary ionic porphyrin nanocomposites. *Chem. Commun.* **2012**, *48*, 4863–4865. [[CrossRef](#)] [[PubMed](#)]
37. Kim, H.J.; Park, K.-M.; Ahn, T.K.; Kim, S.K.; Kim, K.S.; Kim, D.; Kim, H.-J. Novel fullerene–porphyrin–fullerene triad linked by metal axial coordination: Synthesis, X-ray crystal structure, and spectroscopic characterizations of *trans*-bis([60]fullerenoacetato)tin(IV) porphyrin. *Chem. Commun.* **2004**, 2594–2595. [[CrossRef](#)]
38. Kim, H.-J.; Jo, H.J.; Kim, J.; Kim, S.-Y.; Kim, D.; Kim, K. Supramolecular self-assembly of tin(IV) porphyrin channels stabilizing single-file chains of water molecules. *CrystEngComm* **2005**, *7*, 417–420. [[CrossRef](#)]
39. Shee, N.K.; Kim, M.K.; Kim, H.-J. Fluorescent chemosensing for aromatic compounds by supramolecular complex composed of tin(IV) porphyrin, viologen, and cucurbit [8]uril. *Chem. Commun.* **2019**, *55*, 10575–10578. [[CrossRef](#)]
40. Kim, M.K.; Shee, N.K.; Lee, J.; Yoon, M.; Kim, H.-J. Photoinduced Electron Transfer upon Supramolecular Complexation of (Porphyrinato) Sn-Viologen with Cucurbit [7]uril. *Photochem. Photobiol. Sci.* **2019**, *18*, 1996–2002. [[CrossRef](#)]
41. Kim, H.J.; Shee, N.K.; Park, K.M.; Kim, H.-J. Assembly and X-ray crystal structures of heterometallic multiporphyrins with complementary coordination between ruthenium (II) and tin (IV) porphyrins. *Inorg. Chim. Acta* **2019**, *488*, 1–7. [[CrossRef](#)]
42. Shee, N.K.; Lee, C.-J.; Kim, H.-J. Crystal structure of bis (benzoato- κ O)[5,15-di-phenyl-10,20-bis(pyridin-4-yl)porphyrinato- κ^4 N,N',N'',N''']tin(IV). *IUCrData* **2019**, *4*, x190787. [[CrossRef](#)]
43. Shee, N.K.; Lee, C.-J.; Kim, H.-J. Hexacoordinated Sn(IV) porphyrin-based square-grid frameworks exhibiting selective uptake of CO₂ over N₂. *Bull. Korean Chem. Soc.* **2022**, *43*, 103–109. [[CrossRef](#)]
44. Jo, H.J.; Kim, S.H.; Kim, H.-J. Supramolecular Assembly of Tin(IV) Porphyrin Cations Stabilized by Ionic Hydrogen-Bonding Interactions. *Bull. Korean Chem. Soc.* **2015**, *36*, 2348–2351. [[CrossRef](#)]
45. Li, C.; Park, K.-M.; Kim, H.-J. Ionic assembled hybrid nanoparticle consisting of tin(IV) porphyrin cations and polyoxomolybdate anions, and photocatalytic hydrogen production by its visible light sensitization. *Inorg. Chem. Commun.* **2015**, *60*, 8–11. [[CrossRef](#)]
46. Safarik, I.; Safarikova, M. Detection of low concentrations of malachite green and crystal violet in water. *Water Res.* **2002**, *36*, 196–200. [[CrossRef](#)]
47. Seo, H.J.; Lee, J.W.; Na, Y.H.; Boo, J.-H. Enhancement of Photocatalytic Activities with Nanosized Polystyrene Spheres Patterned Titanium Dioxide Films for Water Purification. *Catalysts* **2020**, *10*, 886. [[CrossRef](#)]
48. Guergueb, M.; Brahmi, J.; Nasri, S.; Loiseau, F.; Aouadi, K.; Guerineau, V.; Najmudin, S.; Nasri, H. Zinc(II) triazole meso-aryl substituted porphyrins for UV-visible chloride and bromide detection. Adsorption and catalytic degradation of malachite green dye. *RSC Adv.* **2020**, *10*, 22712–22725. [[CrossRef](#)]
49. Martínez-Chávez, L.A.; Rivera-Muñoz, E.M.; Velázquez-Castillo, R.R.; Escobar-Alarcón, L.; Esquivel, K. Au-Ag/TiO₂ Thin Films Preparation by Laser Ablation and Sputtering Plasmas for Its Potential Use as Photoanodes in Electrochemical Advanced Oxidation Processes (EAOP). *Catalysts* **2021**, *11*, 1406. [[CrossRef](#)]
50. Oliveira, T.P.; Rodrigues, S.F.; Marques, G.N.; Viana Costa, R.C.; Garçone Lopes, C.G.; Aranas, C., Jr.; Rojas, A.; Gomes Rangel, J.H.; Oliveira, M.M. Synthesis, Characterization, and Photocatalytic Investigation of CuFe₂O₄ for the Degradation of Dyes under Visible Light. *Catalysts* **2022**, *12*, 623. [[CrossRef](#)]
51. Gligorovski, S.; Strekowski, R.; Barbati, S.; Vione, D. Environmental Implications of Hydroxyl Radicals (\bullet OH). *Chem. Rev.* **2015**, *115*, 13051–13092. [[CrossRef](#)]
52. Diao, Z.; Li, M.; Zeng, F.; Song, L.; Qiu, R. Degradation pathway of malachite green in a novel dual-tank photoelectrochemical catalytic reactor. *J. Hazard. Mater.* **2013**, *260*, 585–592. [[CrossRef](#)] [[PubMed](#)]
53. Baranowska-Korczyn, A.; Mackiewicz, E.; Ranoszek-Soliwoda, K.; Grobelny, J.; Celichowski, G. Core/Shell Ag/SnO₂ Nanowires for Visible Light Photocatalysis. *Catalysts* **2022**, *12*, 30. [[CrossRef](#)]
54. Wang, H.; Zhang, J.; Yuan, X.; Jiang, L.; Xia, Q.; Chen, H. Photocatalytic removal of antibiotics from natural water matrices and swine wastewater via Cu(I) coordinately polymeric carbon nitride framework. *Chem. Eng. J.* **2020**, *392*, 123638. [[CrossRef](#)]
55. De Luca, G.; Romeo, A.; Scolaro, L.M. Counteranion Dependent Protonation and Aggregation of Tetrakis(4-sulfonatophenyl) porphyrin in Organic Solvents. *J. Phys. Chem. B* **2006**, *110*, 7309–7315. [[CrossRef](#)] [[PubMed](#)]
56. Occhiuto, I.G.; Zagami, R.; Trapani, M.; Bolzonello, L.; Romeo, A.; Castriciano, M.A.; Collini, E.; Monsù Scolaro, L. The Role of Counter-Anions in the Kinetics and Chirality of Porphyrin J-Aggregates. *Chem. Commun.* **2016**, *52*, 11520–11523. [[CrossRef](#)] [[PubMed](#)]